

## Low lattice thermal conductivity with two-channel thermal transport in the superatomic crystal $\text{PH}_4\text{AlBr}_4$

Peng-Hu Du <sup>1</sup>, Cunzhi Zhang <sup>2</sup>, Tingwei Li <sup>1</sup>, and Qiang Sun <sup>1,\*</sup>

<sup>1</sup>*School of Materials Science and Engineering, CAPT, Peking University, Beijing 100871, China*

<sup>2</sup>*Pritzker School of Molecular Engineering, University of Chicago, Chicago, Illinois 60637, USA*



(Received 15 December 2022; accepted 3 April 2023; published 25 April 2023)

Designing novel crystalline materials composed of light and nontoxic elements, but with ultralow thermal conductivity insensitive to temperature, has been a long-standing challenge. One effective strategy is to utilize superatoms as building blocks to introduce hierarchical bonding and vibration for suppressing phonon velocity and enhancing high-order scattering. However, far fewer theoretical efforts have been made to understand the lattice dynamics and thermal transport in superatom-based materials. Herein, different from most of the existing works reported hitherto on atom-superatom hybrid systems, we carry out a comprehensive study on the phonon interaction and thermal transport in superatomic crystal  $\text{PH}_4\text{AlBr}_4$  solely consisting of superatoms (superalkali and superhalogen), by employing homogeneous nonequilibrium molecular dynamics with active-learning potential, combined with density functional theory and unified theory of phonon thermal transport. We find that the supersalt  $\text{PH}_4\text{AlBr}_4$  crystal exhibits amorphouslike ultralow lattice thermal conductivity of  $0.329\text{--}0.286\text{ W m}^{-1}\text{ K}^{-1}$  from 200 to 600 K. In particular, due to the strong quartic anharmonicity, the contribution of four-phonon scattering reaches 38% of total scattering rates at 300 K, while the phonon coherence's contribution is comparable with that of population, resulting from significant phonon localization. These theoretical findings demonstrate that superatom-assembled materials exhibit features distinguished from atom-based crystals and provide a unique platform for exploring ultralow thermal conductivity with enhanced two-channel thermal transport.

DOI: [10.1103/PhysRevB.107.155204](https://doi.org/10.1103/PhysRevB.107.155204)

### I. INTRODUCTION

Materials with low thermal conductivity have diverse applications in thermal insulation, thermal barrier coating, and especially thermoelectric devices [1–3]. According to the Slack rules [4], one can derive the following basic requirements for low lattice thermal conductivity ( $\kappa_{\text{lat}}$ ) [5,6]: strong anharmonicity, complex crystal structure, weak atomic bonds, and large average atomic mass. Previous studies have focused on traditional atom-based compounds which would satisfy these conditions as much as possible to lower the  $\kappa_{\text{lat}}$  [7–9]. However, seeking such materials consisting of light and nontoxic elements but with ultralow  $\kappa_{\text{lat}}$  is still a great challenge. When the design paradigm shifts from elemental atoms to superatoms, the design space and flexibility for thermal materials [10,11] will be tremendously expanded.

“Superatom” refers to a stable atomic cluster composed of multiple atoms with electronic structure and chemical properties similar to that of a single atom in the Periodic Table of elements [12]. By combining atomic precision, synthetic flexibility, and tunable properties, superatoms emerge as versatile building blocks for superatom-based materials that exhibit properties very different from those constructed from individual atoms [13–15]. It is well known that superatomic crystals have two characteristic length scales: the interatomic

distance inside superatoms and the intersuperatomic spacing, thus forming rich bonding hierarchies [12,16], which are much more complex than that in the “rattler-type” materials such as clathrates [17,18] and skutterudites [19,20]. As a result, the coupling of intrasuperatom and intersuperatom modes (hierarchical vibration) significantly affects lattice dynamics and phonon thermal transport [11,21]. Experimentally, various superatomic crystals have been successfully synthesized from metal chalcogenide [11,22–24] or boride clusters [25,26], fullerenes [27–29], and elemental polyhedrons [30], which can exhibit ultralow  $\kappa_{\text{lat}} < 1\text{ W m}^{-1}\text{ K}^{-1}$ . However, because of the limitation of current experimental measurements, theoretical calculations are needed to help better understand the microscopic mechanisms of phonon transport in these superatomic crystals. So far, such theoretical studies have been challenging due to the structural complexity, chemical bonding hierarchy, and especially phonon multichannel thermal transport mechanisms.

Among the reported superatoms, the superhalogen and superalkali are of special interest in developing supersalts where superatoms retain their structural and compositional identity [31]. Currently, the studies on supersalts mainly focus on stability and electronic properties, while far fewer efforts have been made on phonons and thermal properties. Such a situation is gradually changing due to the better understanding of supersalts as a unique platform for phonon transport. Recently, Li *et al.* [32] theoretically studied the heat transfer in a  $\text{NaNO}_3$  monolayer composed of superhalogen  $\text{NO}_3$ , where

\*sunqiang@pku.edu.cn

strong four-phonon scattering leads to a 60% reduction in  $\kappa_{\text{lat}}$  at 300 K; Du *et al.* [33] calculated phonon transport in a superionic conductor  $\text{Na}_3\text{OBH}_4$  consisting of superhalogen  $\text{BH}_4$  and found that the contribution of four-phonon scattering increases 13%–32% when the temperature rises from 200 to 400 K.

However, these theoretical studies [32–34] have the following limitations: (i) the focused systems were atoms and superatoms mixed, instead of being solely superatom based; (ii) the reported results did not include the coherence thermal transport that could be important in superatom-based materials due to the complex structure and strong anharmonicity. Therefore, it is highly desired to explore how important the four-phonon scattering and diffusion thermal transport are in superatomic crystals composed *entirely of superatoms*, which motivates us to carry out this theoretical work by taking supersalt  $\text{PH}_4\text{AlBr}_4$  as an example that consists of both the superalkali  $\text{PH}_4$  and superhalogen  $\text{AlBr}_4$  proposed recently [35].

## II. COMPUTATIONAL METHODS

### A. Structural and electronic properties

Structural and electronic properties of  $\text{PH}_4\text{AlBr}_4$  are calculated by VASP [36] based on the density functional theory (DFT). The projected augmented wave method [37,38] and PBEsol [39] exchange-correlation functional are used. The plane-wave energy cutoff is 400 eV and the convergence criterion of total energy in electronic self-consistent iterations is  $1 \times 10^{-8}$  eV. Both the atomic positions and the lattice constants are allowed to relax until the maximal residual Hellmann-Feynman forces on atoms are smaller than  $1 \times 10^{-5}$  eV/Å. A  $7 \times 7 \times 7$   $k$  mesh for primitive cell with a  $\Gamma$ -centered Monkhorst-Pack scheme and van der Waals (vdW) interaction correction with the DFT-D3 method with zero-damping function [40] are adopted. The tests for plane-wave cutoff and  $k$ -mesh sampling in the first Brillouin zone (BZ) are performed, respectively (Fig. S1 in the Supplemental Material [41]). All the *ab initio* molecular dynamics (AIMD) simulations are  $\Gamma$ -only performed with zero-temperature lattice parameters and a time step of 1.5 fs under the canonical ensemble (*NVT*) using the Nosé-Hoover thermostat.

### B. Machine-learning potential and molecular dynamics

*Data sets.* DFT calculations are used to prepare the training and test data, on which a neural network-based machine-learning potential (NEP) [42] is trained for  $\text{PH}_4\text{AlBr}_4$ . The initial dataset consists of 550 cells, each with 240 atoms, among which 400 tetragonal cells are sampled uniformly from AIMD trajectories with temperatures of 300, 500, 700, and 1000 K as described above. To sample the local density fluctuation, 50 distorted cells, 50 volumetric compressed cells, and 50 volumetric stretched cells are generated with random atomic displacements using the HIPHIVE package [43]. Static self-consistent calculations are performed to obtain accurate energy, force, and virial data by using the same setting as above except for a sparser  $1 \times 1 \times 1$   $k$  mesh for speedup.

*Training processes.* All the tunable hyperparameters used for the NEP potential are listed in Table I, among which we specially choose large interaction cutoffs considering the vdW

TABLE I. All the tunable hyperparameters used in NEP potential for  $\text{PH}_4\text{AlBr}_4$ .  $r_c^R$  ( $r_c^A$ ) is the cutoff radius (Å) for the radial (angular) components of the descriptor,  $n_{\text{max}}^R$  ( $n_{\text{max}}^A$ ) is the Chebyshev polynomial expansion order for the radial (angular) components,  $l_{\text{max}}$  is the Legendre polynomial expansion order for the angular components,  $N_{\text{neu}}$  is the number of neurons in the only hidden layer of the artificial network work,  $\lambda_1$  ( $\lambda_2$ ) is the  $\mathcal{L}_1$  ( $\mathcal{L}_2$ ) regularization parameter,  $N_{\text{pop}}$  is the population size in the natural evolution strategy algorithm, and the  $N_{\text{gen}}$  is the maximum number of generations to be evolved.

Parameter	Value	Parameter	Value
$r_c^R$	8	$N_{\text{neu}}$	50
$r_c^A$	4	$\lambda_1$	0.05
$n_{\text{max}}^R$	12	$\lambda_2$	0.05
$n_{\text{max}}^A$	6	$N_{\text{pop}}$	50
$l_{\text{max}}$	4	$N_{\text{gen}}$	$\sim 2.7 \times 10^5$

and Coulomb interactions in DFT data. Figure S2 [41] shows the evolution of various loss functions with respect to the generation for our initial NEP model, where the root mean square errors (RMSEs) of energy, force, and virial are reduced and converged with increasing generations.

*Active learning.* Although the accuracy of the initial NEP model (Fig. S3 [41]) has reached an acceptable level in terms of numerical errors, the trajectories of long-time MD simulations may be beyond the boundary of the training sample space [Figs. 1(a) and 1(b)]. To further improve the initial model and stabilize subsequent large-scale runs, we introduce an active-learning strategy by selecting unsampled configurations from the NEP-MD trajectories and training new models on the expanded dataset [Figs. 1(c) and 1(d)]. We find that the scheme of model inheritance from the initial one (total loss of 0.0770) is superior to the *ab initio* training (0.0837) within the same training time, which benefits from better

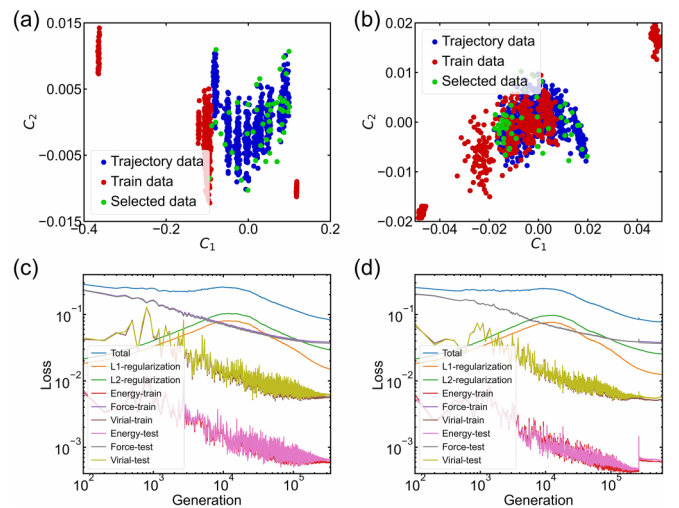


FIG. 1. Active-learning processes for improving the initial NEP model. Data distribution depicted on a two-dimensional space ( $C_1$  and  $C_2$ ) after principal component analysis, where trajectory data are from NEP-MD simulations under (a) *NPT* and (b) *NVT* ensemble with a series of temperatures; evolution of the loss functions during (c) *ab initio* and (d) inheritance training process of new NEP models.

parameter initialization after a pretraining undertaken by the initial model.

**Molecular dynamics simulations.** The homogeneous nonequilibrium molecular dynamics and the related spectral decomposition methods [44] with NEP potential as implemented in the GPUMD package [45,46] are used to simulate the lattice thermal conductivity. We use an approximately cubic simulation cell with a volume of  $84.23 \times 84.23 \times 81.67 \text{ \AA}^3$  (30 000 atoms) for  $\text{PH}_4\text{AlBr}_4$ , which is sufficiently large to eliminate finite-size effects. Periodic boundary conditions are applied in all directions and a small time step of 0.1 fs is used due to the light H atoms. We perform five independent runs, 200 ps for equilibrium in the *NVT* ensemble with the Berendsen thermostat, and then 2000 ps for production in the *NVT* ensemble with the Nosé-Hoover thermostat under an external force ( $F_e$ ) of  $1.0 \times 10^{-3} \text{ \AA}^{-1}$ . We choose a temperature range from 200 to 700 K for  $\text{PH}_4\text{AlBr}_4$ , and calculate the cumulative average  $[\kappa_{\text{ave}}^{\text{zz}}(t)]$  of the obtained running thermal conductivity  $[\kappa^{\text{zz}}(t)]$  for better convergence (Fig. S5 [41]); then the ultimate value of NEP-MD simulated  $\kappa_{\text{lat}}^{\text{zz}}$  (labeled as  $\kappa_{\text{MD}}^{\text{zz}}$ ) is based on the average result of the last 1000 ps simulations for five individual MD runs. It should be noted that the parameter  $F_e$  is crucial; it has to be small enough to keep the system within the linear-response regime and large enough to retain a sufficiently large signal to noise ratio. The tests are carried out carefully for  $F_e$ , the simulation cell, and time used in NEP-MD (Figs. S6–S8 [41]).

### C. Force constants and phonon properties

Lattice dynamics and phonon transport properties are calculated in a  $2 \times 2 \times 3$  tetrahedral supercell with 240 atoms. The second, third, and fourth interatomic force constants (IFCs) are efficiently extracted by training a force constants potential (FCP) based on a DFT dataset containing 60 configurations with random atomic displacements generated by the Monto Carlo rattle procedure using the HIPHIVE package, where the least-squares fitting method is used with the cutoff radius of 8.41, 5.0, and 4.0  $\text{\AA}$  for second, third, and fourth IFCs, respectively. The second IFCs are also calculated based on finite-enumerated displacements in the PHONOPY package [47] as a benchmark. The hyperparameters tuned for training the FCP model and its optimal accuracy are displayed in Figs. S10 and S11 [41]. Phonon spectra are calculated with 101  $q$  points for each segment along the high-symmetry path in the BZ, and the density of states with a  $q$  mesh of  $30 \times 30 \times 30$ . Elastic moduli are determined by performing finite lattice distortions and deriving the elastic constants from the strain-stress relationship [48]. The Debye temperature is obtained simply from the elastic constants [49].

The population's part ( $\kappa_P$ ) of the lattice thermal conductivity for  $\text{PH}_4\text{AlBr}_4$  is further calculated by solving the phonon Boltzmann transport equation using the SHENGBTE package [50] with FOURPHONON code [51]. Scattering rates are computed including three-phonon (3ph) through the self-consistent iterative approach and four-phonon (4ph) scattering under the relaxation time approximation. The convergence of  $\kappa_P$ , a  $3 \times 3$  tensor, with respect to the size of the  $q$  mesh and Gaussian smearing is tested carefully (Figs. S12(a) and S12(b) [41]). To balance the memory demand and convergence ef-

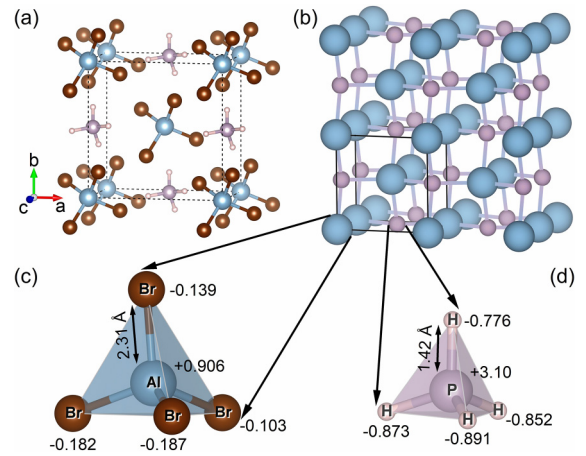


FIG. 2. Crystallographic structure of  $\text{PH}_4\text{AlBr}_4$ . (a) Unit cell with the body-centered tetragonal lattice; (b) assembly model with each superatom simplified as a sphere; tetrahedral block of (c) superhalogen  $\text{AlBr}_4$  and (d) superalkali  $\text{PH}_4$ . Bader effective charges of each atom and averaged Al-Br and P-H bond lengths in a formula unit are labeled.

iciency, we use a relatively dense  $q$  mesh of  $10 \times 10 \times 10$  and a scale parameter for Gaussian smearing of 1.0 for 3ph only, and 0.01 with significant speedups but a negligible loss of precision when 4ph processes are included. The nonanalytical correction has little influence on the magnitude of  $\kappa_P^{\text{zz}}$  (Fig. S12(c) [41]), and thus is not considered throughout the  $\kappa_P$  investigation. To obtain further speedup, we compute the scattering rates for phonons with frequency  $< 15$  THz, while the modes of higher frequency are ignored due to their minor contributions to  $\kappa_{\text{lat}}^{\text{zz}}$  as revealed by the NEP-MD results.

## III. RESULTS AND DISCUSSION

### A. Hierarchical structures of $\text{PH}_4\text{AlBr}_4$

From the whole family of supersalts proposed previously [35], we take  $\text{PH}_4\text{AlBr}_4$  [Fig. 2(a)] as a case study, which consists of both superalkali  $\text{PH}_4$  and superhalogen  $\text{AlBr}_4$  with the stoichiometric ratio of 1:1 in a body-centered tetragonal lattice with  $I\bar{4}$  (No. 82) space group. The relaxed lattice constants are  $a = b = 8.42 \text{ \AA}$ ,  $c = 5.45 \text{ \AA}$  for the unit cell with four Wyckoff sites (Table S1 [41]). As depicted in Figs. 2(b)–2(d), although each superalkali  $\text{PH}_4$  is coordinated by four superhalogen  $\text{AlBr}_4$  and vice versa (namely, distorted zincblende framework [35]), all superatoms are slightly distorted deviating from the regular tetrahedron ( $T_d$  point group) that appears in a free state.

To investigate the chemical bonding features of  $\text{PH}_4\text{AlBr}_4$ , the electron localization function [52] is depicted in Fig. 3(a) and Fig. S13 in the Supplemental Material [41]. The results reveal that valence electrons are substantially localized around H and Br atoms (superatomic peripheral atoms with negative charges) while they are farther away from P and Al atoms (central atoms with positive charges), which is consistent with the Bader charges labeled in Figs. 2(c) and 2(d). Then we analyze the crystal orbital Hamiltonian populations (COHPs) [53], as shown in Fig. 3(b), where the dimensionless  $-\text{COHP} > 0$  means bonding while  $< 0$  means antibonding.

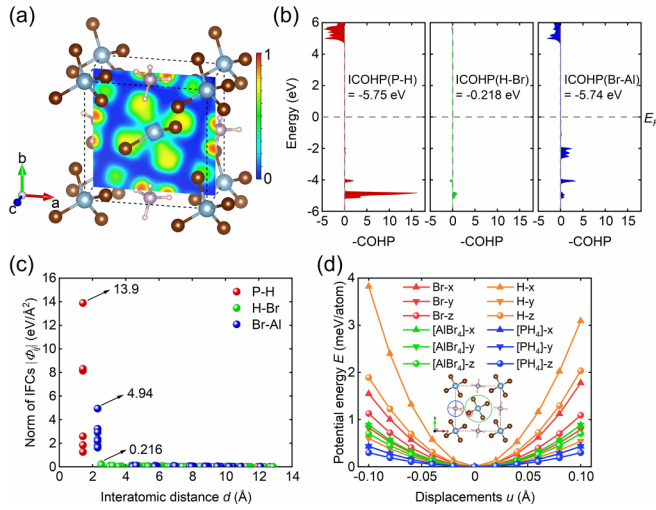


FIG. 3. Chemical bonding of  $\text{PH}_4\text{AlBr}_4$ . (a) Electron localization function depicted by the 2D cross section; (b) COHP decomposed to P-H, H-Br, and Br-Al atomic pairs; (c) norm of second interaction force constants as a function of interatomic distance; (d) potential energy surface with respect to displacements of Br and H single atom, and  $\text{AlBr}_4$  and  $\text{PH}_4$  clusters along the  $x$ ,  $y$ , and  $z$  directions, respectively. The solid lines are a guide to the eyes.

One can see that all the occupied states are substantially contributed by P-H and Br-Al bonding interactions but only a few

H-Br antibonding components. The energy-integrated COHP (ICOHP) up to Fermi level, by summing over all the bonding, nonbonding, and antibonding interactions, illustrates that the internal cluster bonding strengths of  $-5.75$  and  $-5.74$  eV for  $\text{PH}_4$  and  $\text{AlBr}_4$ , respectively, are much larger than the intercluster bonding of  $-0.218$  eV for H-Br. The distinct bonding hierarchy, namely, very strong intrasuperatom bonds but only weak intersuperatom interactions, is further confirmed by the norm of second interatomic force constants (IFCs) in Fig. 3(c), where the IFCs of the P-H (Br-Al) pair are about 64 (23) times larger than those of H-Br.

In addition, by monitoring the potential energy surface (PES) with respect to displacements of atoms or superatoms [Fig. 3(d)], we note that the PESs of a single H (Br) atom are inequivalent among three directions, exhibiting an obvious anisotropic character. It is also observed that the  $\text{PH}_4$  cluster exhibits nearly zero restoring force for a wide displacement range, implying a large thermal motion and remarkable anharmonicity. Specifically, both cubic and quartic anharmonic terms play roles in the interaction of superatomic peripheral atoms, while quartic anharmonicity is more essential for the whole superatom (Fig. S14 [41]).

## B. Lattice dynamics

Because lattice thermal conduction is closely related to phonon properties, we first calculate the harmonic phonon (HP) dispersions using the supercell method. In Fig. 4(a), the

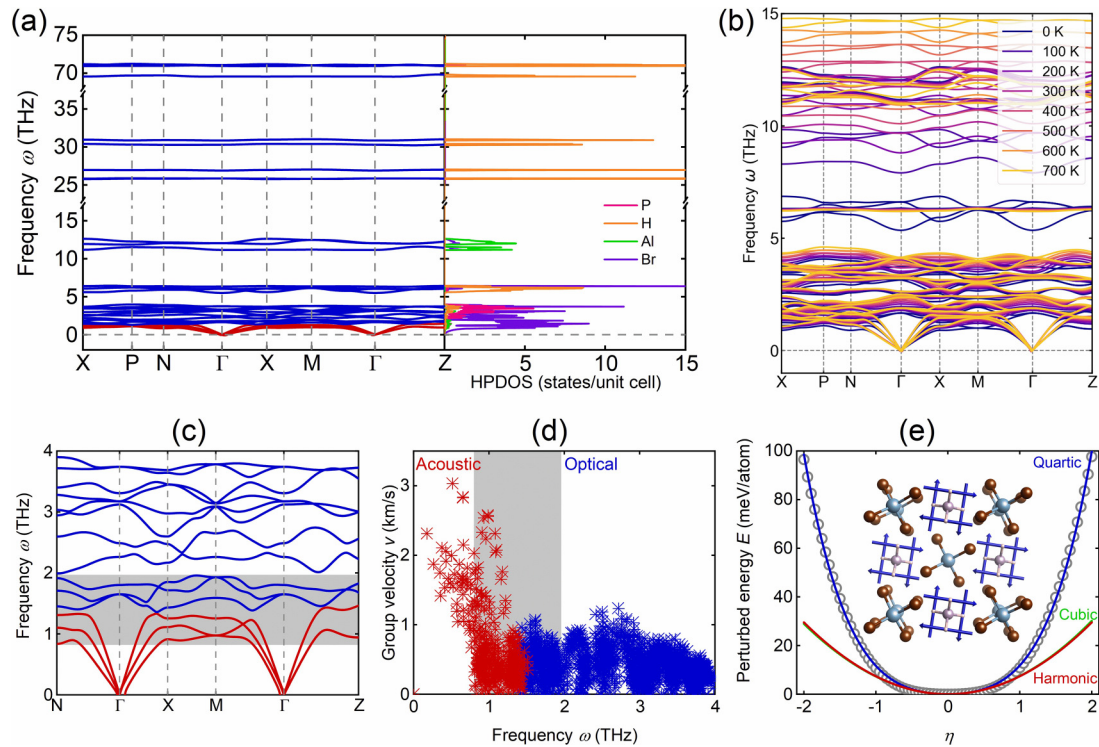


FIG. 4. Lattice dynamics of  $\text{PH}_4\text{AlBr}_4$ . (a) Harmonic phonon spectrum and atom-projected harmonic phonon DOS; (b) finite-temperature phonon dispersions from SCP calculations; (c) detailed phonon dispersions in the low-frequency range; (d) phonon mode resolved group velocity. In (a,c,d), the red and blue correspond to acoustic and optical modes, respectively. In (c,d), the shadowed area marks those avoided-crossing modes. (e) Frozen phonon-perturbed potential of phonon mode  $\Gamma_{15}$  with  $\omega = 5.50$  THz and its quadratic (harmonic), cubic, and quartic fitting. The inset is superatomic rotation mode, where the arrows through the H atoms represent atomic displacements for the corresponding phonon eigenvector.

highest phonon frequency exceeds 70 THz deriving from the H-P vibrations within superalkalis, as resolved by the atom-projected phonon density of states (PDOS). However, the acoustic phonon modes with only  $\omega < 1.5$  THz, mainly contributed by the Br atoms, strongly overlap with a large number of low-lying optical branches and gradually flatten out. Accordingly, their propagation velocities are severely suppressed and drop notably with increasing frequency [Fig. 4(d)], due to the avoided crossing with the optical modes where the acoustic branches start to bend with nonlinear dispersions away from the center of the BZ [54] [details in Fig. 4(c)]. As discussed in the section about elastic properties in the SM [41] (see, also, Refs. [55–60] therein), the Young's modulus of  $\text{PH}_4\text{AlBr}_4$  is only 23.5 GPa, suggesting its nature of softness; thus  $\theta_D$  is only 206 K, even lower than that of atom-based soft lattices such as  $\text{Ag}_2\text{S}$  (258 K [61]) and  $\text{Cu}_2\text{S}$  (237 K [62]).

In addition, the optical branches with  $\omega > 5$  THz exhibit distinct splitting of phonon frequency with large gaps, corresponding to intensely localized vibrations with small phonon participation ratio  $< 0.5$  (Fig. S15(a) [41]). In particular, those phonon branches with  $\omega > 15$  THz are nearly flat with dense PDOS, which are substantially contributed by H and P atoms involving the internal vibrations of superalkali  $\text{PH}_4$ , leading to extremely low phonon group velocity ( $< 0.6$  km/s in Fig. S15(b) [41]). Those sharp peaks located at the frequency of flat branches in the PDOS represent Van Hove singularities that may derive from localized phonon modes induced by atomic disorder [63,64], here implying the intrasuperatom variation in shape and orientation.

Moreover, the acoustic phonons coupled with optical modes ( $\omega = 1\text{--}2$  THz), and the flat optical branches ( $\omega = 5\text{--}10$  THz) contributed by H and Br atoms, exhibit extremely large Grüneisen parameters with negative values (Fig. S15(c) [41]), comparable with some low- $\kappa_{\text{lat}}$  compounds possessing lone-pair electrons [65,66]. This verifies the strong lattice anharmonicity in  $\text{PH}_4\text{AlBr}_4$ , which is possibly enhanced by intersuperatom non- and antibonding components of H-Br interaction. In this regard, we perform the frozen phonon-perturbed calculation for the 15th mode at the  $\Gamma$  point ( $\omega = 5.50$  THz), depicted in Fig. 4(d), which is fit badly to a quadratic potential but very well to a quartic well, implying the predominant quartic anharmonicity in the rotation of superatoms.

Since we are dealing with a soft material, the temperature effects need to be considered. By using the self-consistent phonon (SCP) method [67,68] for renormalization, we first obtain finite-temperature phonon dispersions [Fig. 4(b)], where no imaginary frequency is observed at higher temperatures, confirming its reliable dynamic stability. It is also noted that low-frequency phonons harden gradually with increasing temperature, especially for the optical phonon branches with  $\omega > 5$  THz.

We then perform *ab initio* molecular dynamics (AIMD) simulations to capture the real-time atomic motions in  $\text{PH}_4\text{AlBr}_4$ . As displayed in Fig. 5(a) and Fig. S16 in the Supplemental Material [41], the potential energy of the simulated system oscillates around the stable average, suggesting the thermal stability of  $\text{PH}_4\text{AlBr}_4$  exceeding 700 K. However, we note the stability analysis here is a crude estimate given the relatively short time and small supercell. The

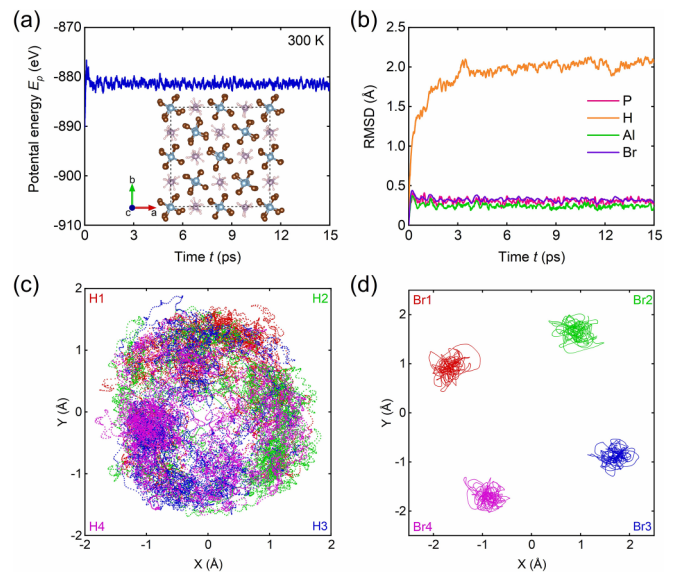


FIG. 5. AIMD simulations at 300 K for  $\text{PH}_4\text{AlBr}_4$ . (a) The evolution of potential energy of a  $2 \times 2 \times 3$  supercell during the simulations and a snapshot of the equilibrium structure (inset) at the end of 15 ps; (b) atom-resolved root mean square displacements with respect to simulation time; (c,d) simulation trajectories projected onto the  $x$ - $y$  plane for peripheral atoms of tetrahedral superatoms, i.e., four H and Br atoms, respectively.

superalkali  $\text{PH}_4$  and superhalogen  $\text{AlBr}_4$  remain intact [inset in Fig. 5(a)], while the loosely bound  $\text{PH}_4$  shows random rotation and dynamic disordered orientation. The superatomic rotation is evidently demonstrated in Figs. 5(c) and 5(d), where the projected trajectories of four corner H atoms of tetrahedral superalkali overlap each other, which is different from the separable trajectories of Br atoms of superhalogen. As a simple estimation, the timescale in which one rotation of  $\text{PH}_4$  cluster happens is about 2.68 ps (Fig. S17 [41]). This unique vibrational character is substantiated further by the root mean square displacements (RMSDs) in Fig. 5(b), where the H atom exhibits remarkable displacements and requires a longer time to reach a thermodynamic stability state than others, indicating the asynchronous phenomenon arising from the hierarchical structure. Detailed in Fig. S18 [41], the spatial trajectories of the peripheral H and Br atoms are more dispersive than the central atoms (P and Al), confirming the existence of hierarchical lattice vibration.

### C. Lattice thermal conductivity from NEP-MD

Due to the hierarchically bonded structure and complex lattice vibration, the computation of lattice thermal conductivity ( $\kappa_{\text{lat}}$ ) in the solely superatomic crystal is challenging. Herein, we combine the molecular dynamics (MD) simulations and machine-learning potentials for accurate prediction of  $\kappa_{\text{lat}}$  [69]. Since the well-trained NEP potential shows reasonably good agreement with DFT as evaluated by prediction RMSE and phonon dispersions (Fig. S4 [41]), it is reliable to use it for producing generalized PES to simulate macroscopic thermal conduction with large-size and long-time MD. The total  $\kappa_{\text{lat}}$  of  $\text{PH}_4\text{AlBr}_4$  is determined by using the homogeneous

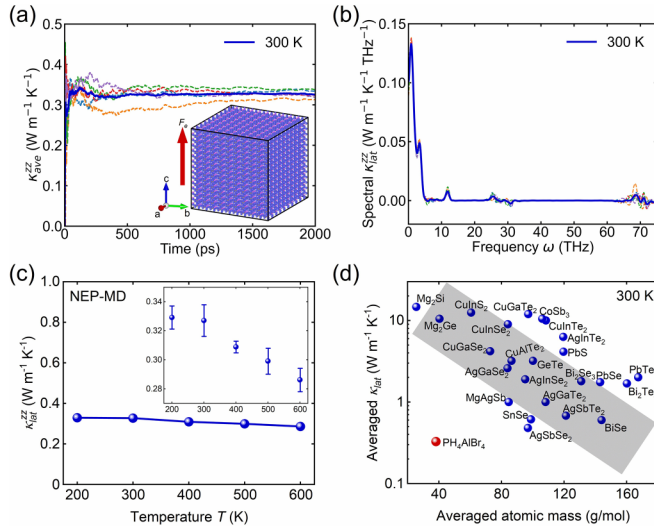


FIG. 6. Total lattice thermal conductivity of  $\text{PH}_4\text{AlBr}_4$  simulated by NEP-MD. (a) Cumulative average of the running thermal conductivity  $\kappa_{\text{ave}}^{\text{zz}}(t)$  as a function of time and (b) spectral thermal conductivity at 300 K. The inset in (a) is a simulation cell with 30 000 atoms; the arrow represents the direction of external force. In (a,b), the dashed lines are from individual runs and the solid line is their average. (c) Temperature dependence of ultimate lattice thermal conductivity  $\kappa_{\text{MD}}^{\text{zz}}$ , where the error bars in the inset are the standard deviation for five individual runs; (d)  $\kappa_{\text{lat}}$  at room temperature versus averaged atomic mass, where the gray stripe denotes the general inverse relationship between them.

nonequilibrium MD method with the NEP potential (denoted as NEP-MD), as illustrated in Fig. 6.

The cumulative average of running thermal conductivity [ $\kappa_{\text{ave}}^{\text{zz}}(t)$ ] for a model system with 30 000 atoms [inset in Fig. 6(a)] well converges for long-time simulations up to 2000 ps from 200 to 600 K (Fig. 6(a) and Fig. S9 in the Supplemental Material [41]), whereas the system collapses when the temperature reaches around 700 K (overestimated by AIMD). Specifically, the ultimate average value of  $\kappa_{\text{lat}}^{\text{zz}}$  from NEP-MD (labeled as  $\kappa_{\text{MD}}^{\text{zz}}$ ) is as low as  $0.327 \text{ W m}^{-1} \text{ K}^{-1}$  at 300 K despite the small averaged atomic mass (38.2 g/mol), which is even lower than that of SnSe ( $0.613 \text{ W m}^{-1} \text{ K}^{-1}$ ) [1], AgSbSe<sub>2</sub> ( $0.48 \text{ W m}^{-1} \text{ K}^{-1}$ ) [65], and BiSe ( $0.60 \text{ W m}^{-1} \text{ K}^{-1}$ ) [70], as compared in Fig. 6(d). From the spectral thermal conductivity [Fig. 6(b)], one can notice that the phonon modes with  $\omega < 5$  THz make major contributions to the  $\kappa_{\text{MD}}^{\text{zz}}$  (92.5%), while the high-frequency ( $\omega > 15$  THz) modes from intrasuperatom vibrations generally do not conduct much heat. Interestingly, the  $\kappa_{\text{lat}}$  in the temperature range from 200 to 600 K [Fig. 6(c)] remains ultralow and exhibits weak temperature dependence, slightly decreasing from 0.329 to  $0.286 \text{ W m}^{-1} \text{ K}^{-1}$ . This demonstrates that the supersalt crystal exhibits an amorphouslike thermal transport characteristic above 200 K, which is attributed to its natures of soft lattice, strong anharmonicity, and hierarchical vibration due to the complex structural and bonding hierarchy.

To benchmark the NEP-MD results, we refer to the theoretical minimum lattice thermal conductivity ( $\kappa_{\text{min}}$ ) which is calculated by the diffuson model proposed by Allen *et al.* [71]

and Feldman *et al.* [72]:

$$\kappa_{\text{min}} = 0.76n^{\frac{2}{3}}k_B\frac{1}{3}(2v_t + v_l),$$

where  $n$  is the number density of atoms;  $v_t$  and  $v_l$  are the transverse and longitudinal wave velocities from elastic moduli. By treating the superalkali  $\text{PH}_4$  and superhalogen  $\text{AlBr}_4$  as effective atoms, the superatom-based  $\kappa_{\text{min}}$  is found to be  $0.107 \text{ W m}^{-1} \text{ K}^{-1}$  as a reasonable lower limit. Additionally, the nearly temperature-independent  $\kappa_{\text{lat}}$  is similar to that observed in disordered systems [73,74]. According to the unified theory of lattice thermal transport in crystals and glasses [75], the total  $\kappa_{\text{lat}}$  includes contributions from particlelike propagation (population's part,  $\kappa_P$ ) and wavelike diffusion (coherence's part,  $\kappa_C$ ). However, the  $\kappa_P$  and  $\kappa_C$  components cannot be resolved with MD simulations. To obtain more detailed insight into the thermal transport in  $\text{PH}_4\text{AlBr}_4$ , as well as supersalt crystals in general, we further calculate the phonon scattering and diffusion based on the perturbation theory (PT). However, particularly due to the complex rotation of superatoms, using PT for thermal conduction calculations probably has limitations, because the PT framework assumes that all atoms vibrate near their respective equilibrium positions. Therefore, we adopt the PT results for qualitatively understanding the heat conduction mechanisms at the model level.

#### D. Phonon scattering and diffusion thermal transport

When first using constant second IFCs under harmonic approximation (HA) and only considering three-phonon (3ph) scattering [HA+3ph in Fig. 7(a)], the calculated  $\kappa_P$  well satisfies  $\kappa^{xx} = \kappa^{yy} > \kappa^{zz}$ , whereas  $\kappa_P$  is incredibly reduced by one order of magnitude when four-phonon (4ph) scattering is included (HA+3ph+4ph), e.g., from  $0.216$  to  $0.034 \text{ W m}^{-1} \text{ K}^{-1}$  at 300 K, which even approaches the thermal conductivity of air ( $0.026 \text{ W m}^{-1} \text{ K}^{-1}$  at 300 K) [76]. Moreover, the calculated  $\kappa_P$  in this way is much lower than the NEP-MD predictions and even  $\kappa_{\text{min}}$  [Fig. 7(a)]. Therefore, more advanced treatment of phonon transport is required.

The next step forward is to use the second IFCs renormalized by the SCP method to take into account the influence of phonon dispersions altered by temperature. This results in a remarkable increase of  $\kappa_P$  when considering either only 3ph scattering (SCP+3ph) or both 3ph and 4ph processes (SCP+3ph+4ph), which are on the same order of magnitude as that of NEP-MD. This primarily originates from the evident weakening of anharmonic scattering (Fig. 7(e) compared with Fig. S19 in the Supplemental Material [41]) due to the shrinkage of phase space. In addition, low-frequency phonons, the main heat-carrying modes, harden due to the temperature effect observed in Fig. 5(b), leading to the increased group velocity with evaluated temperature [Fig. 7(c)].

We note again a significant reduction in the population's thermal conductivity after considering 4ph scattering processes. At 300 K,  $\kappa_P$  drops from  $0.517$  to  $0.321 \text{ W m}^{-1} \text{ K}^{-1}$  with a decreasing amplitude up to 38% [Fig. 7(b)] and approaches the  $\kappa_{\text{min}}$  at higher temperatures, which indicates the strong 4ph scattering strength induced by quartic anharmonicity. As shown in Figs. 8(e) and 8(f), the 4ph scattering rates are comparable with that of 3ph in the low-frequency range

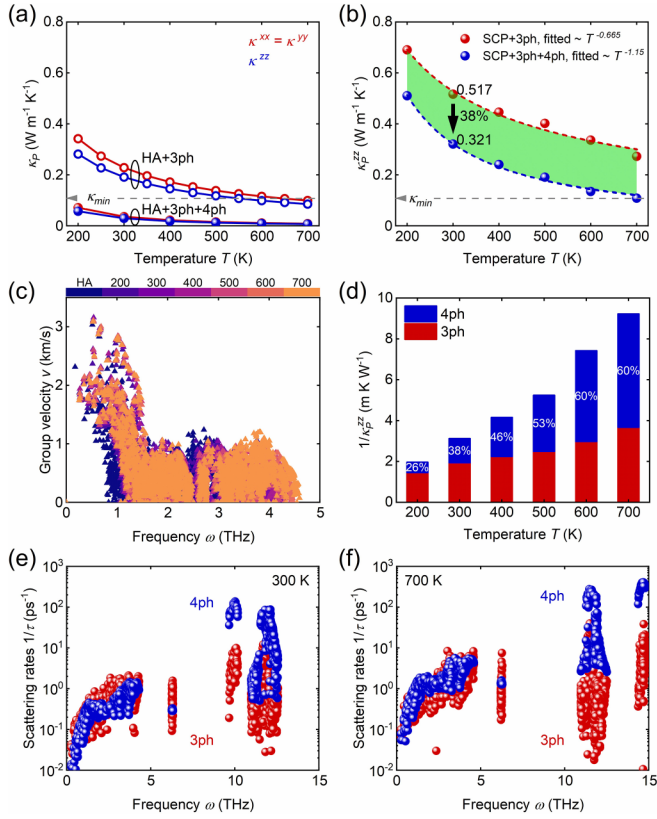


FIG. 7. Phonon scattering properties of  $\text{PH}_4\text{AlBr}_4$ . The phonon population's thermal conductivity as a function of temperature (a) under harmonic approximation and (b) using self-consistent phonon; (c) phonon mode resolved group velocity; (d) three- and four-phonon contributions to total scattering rates where the labeled percentages represent four-phonon proportions; mode-resolved three-phonon (red) and four-phonon (blue) scattering rates at (e) 300 K and (f) 700 K, respectively.

( $\omega < 5$  THz), especially in the avoided crossing region, and even one order of magnitude higher for those dense localized optical modes at 300 K. Up to 700 K, 4ph scattering is rapidly enhanced beyond that of 3ph, due to the stronger dependence on phonon population ( $n$ ) of  $1/\tau_{4\text{ph}} \sim n^2$  [69,77], which increases with  $T$  according to the Bose-Einstein distribution. Accordingly, the relatively weak temperature dependence of  $\kappa_P$  ( $T^{-0.665}$ ) for only 3ph scattering turns into  $T^{-1.15}$  when 3ph and 4ph processes are included simultaneously [Fig. 7(b)], steeper decay with temperature that is different from the conventional relationship of  $T^{-1}$  for most atom-based materials [78,79]. We observe that the lifetimes of 93.2% phonon modes are shorter than the  $\text{PH}_4$  rotation timescale, such that the superatomic rotation may not be fast enough to completely break down the phonon propagation, which would justify the use of PT for qualitative analysis. From the comparison between 3ph and 4ph contributions to total scattering rates in Fig. 7(d), one can conclude that the 4ph interaction processes are important for supersalt  $\text{PH}_4\text{AlBr}_4$  not only at elevated temperatures but also in low ranges.

Furthermore, it is worth noting that the phonon mean free paths (MFPs) of many modes are on the order of interatomic distances [Fig. 8(a)], known as the Ioffe-Regel limit [73].

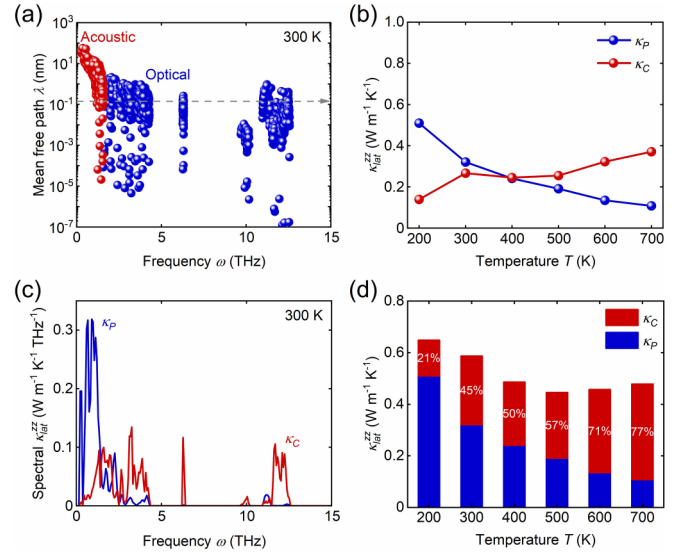


FIG. 8. Diffusion behavior of supersalt  $\text{PH}_4\text{AlBr}_4$ . (a) Phonon mean free paths at 300 K, where the gray dashed line shows the Ioffe-Regel limit; (b) lattice thermal conductivity from unified theory as a function of temperature; (c) spectral decomposition of the population's and coherence's thermal conductivity at 300 K; (d) comparison of contributions to the lattice thermal conductivity from  $\kappa_P$  and  $\kappa_C$ .

Consequently, the thermal transport in this situation will show distinct diffusion behavior. The coherence's thermal conductivity ( $\kappa_C$ ) can be formulated as [74,75]

$$\kappa_C^{\alpha\beta} = \frac{\hbar^2}{k_B T^2} \frac{1}{V_c N_c} \sum_{\mathbf{q}} \sum_{s \neq s'} \frac{\omega(\mathbf{q})_s + \omega(\mathbf{q})_{s'}}{2} \mathcal{V}^\alpha(\mathbf{q})_{s,s'} \mathcal{V}^\beta(\mathbf{q})_{s',s} \times \frac{\omega(\mathbf{q})_s \bar{N}(\mathbf{q})_s [\bar{N}(\mathbf{q})_s + 1] + \omega(\mathbf{q})_{s'} \bar{N}(\mathbf{q})_{s'} [\bar{N}(\mathbf{q})_{s'} + 1]}{4[\omega(\mathbf{q})_s - \omega(\mathbf{q})_{s'}]^2 + [\Gamma(\mathbf{q})_s + \Gamma(\mathbf{q})_{s'}]^2} \times [\Gamma(\mathbf{q})_s + \Gamma(\mathbf{q})_{s'}],$$

where  $\hbar$  and  $k_B$  are the reduced Planck and Boltzmann constants,  $T$  is the thermodynamic temperature,  $V_c$  and  $N_c$  represent the volume and number of unit cell,  $s$  labels  $3N_{at}$  phonon branches ( $N_{at}$  being the number of atoms in unit cell),  $\omega(\mathbf{q})_s$  are eigenvalues of the dynamical matrix  $D(\mathbf{q})$ ,

$$\mathcal{E}^*(\mathbf{q})_{s,b\alpha} D(\mathbf{q})_{b\alpha,b'\alpha'} \mathcal{E}(\mathbf{q})_{s',b'\alpha'} = \omega^2(\mathbf{q})_s \delta_{s,s'},$$

$\bar{N}(\mathbf{q})_s = \{\exp[\frac{\hbar\omega(\mathbf{q})_s}{k_B T}] - 1\}^{-1}$  is the equilibrium Bose-Einstein distribution,  $\Gamma(\mathbf{q})_s = (V_c N_c)^{-1} A^T(\mathbf{q}, \mathbf{q})_{s,s'}$  is the phonon linewidth, and  $A^T(q, q)_{s,s'}$  is the standard collision operator that accounts for anharmonicity. The velocity matrix is obtained by applying a unitary transformation to phonon group velocity under phonon representation described as

$$\mathcal{V}^\beta(\mathbf{q})_{s,s'} = \mathcal{E}^*(\mathbf{q})_{s,b\alpha} \nabla_{\mathbf{q}}^\beta \sqrt{D(\mathbf{q})_{b\alpha,b'\alpha'}} \mathcal{E}(\mathbf{q})_{s',b'\alpha'}.$$

The calculated  $\kappa_C^{zz}$  [Fig. 8(b)] increases overall with temperature rising, exhibiting a temperature dependence contrary to that of  $\kappa_P$  [69]. At 300 K, the magnitude of  $\kappa_C$  ( $0.267 \text{ W m}^{-1} \text{ K}^{-1}$ ) is comparable with that of  $\kappa_P$  ( $0.321 \text{ W m}^{-1} \text{ K}^{-1}$ ); the former mostly originates from the optical phonon modes with lower MFPs while the latter orig-

inates from acoustic phonons with long MFPs, as indicated by the spectral decomposition of lattice thermal conductivity [Fig. 8(c)]. By comparing the contributions to thermal transport from population and coherence [Fig. 8(d)], we discover that the phonon diffusion is non-negligible even at low temperatures, and becomes significant when temperature rises in the supersalt. This is different from atom-based low- $\kappa_{\text{lat}}$  compounds such as SnSe [80] and TlInTe<sub>2</sub> [81], where the population's contribution is substantially dominant in a wide temperature range. We further argue that the diffusion channel for heat transport should be an important feature in superatom-based crystals, where hierarchical bonding and strong anharmonicity can induce closely packed phonon modes.

#### IV. CONCLUSION

In summary, we have conducted a theoretical study on the phonon and thermal properties of supersalt PH<sub>4</sub>AlBr<sub>4</sub> and obtained the following conclusions: (1) Going beyond the previous studies on atom-superatom hybrid systems, PH<sub>4</sub>AlBr<sub>4</sub> is a solely superatom-based crystal composed of superalkali and superhalogen. When a single atom is replaced by a superatom, the structural and bonding hierarchies are significantly enhanced and the geometric configuration becomes much

more complex due to the hierarchical vibration and rotation as well as the relative orientation between superatoms, resulting in strong four-phonon scattering; (2) different from most of the studies reported hitherto on the thermal transport of superatom-based systems by only considering three- and/or four-phonon scattering, we studied the contribution of phonon coherence to the lattice thermal conductivity in a superatomic crystal entirely with superatoms as the building units, and we found that the diffusion thermal transport is greatly enhanced as compared to that of conventional atomic crystals. Our work would help better understand the effect of complex hierarchical structure, four-phonon interaction, and the diffusion channel on the lattice thermal conductivity of superatom-based materials.

#### ACKNOWLEDGMENTS

This work is partially supported by grants from the National Natural Science Foundation of China (Grant No. NSFC-21973001) and from the Ministry of Science and Technology of China (Grant No. 2021YFB4000601). Calculations were performed on the High Performance Computing Platform of Peking University, China.

The authors declare no competing financial interest.

- 
- [1] L. D. Zhao, S. H. Lo, Y. Zhang, H. Sun, G. Tan, C. Uher, C. Wolverton, V. P. Dravid, and M. G. Kanatzidis, Ultralow thermal conductivity and high thermoelectric figure of merit in SnSe crystals, *Nature (London)* **508**, 373 (2014).
  - [2] G. Tan, L. D. Zhao, and M. G. Kanatzidis, Rationally designing high-performance bulk thermoelectric materials, *Chem. Rev.* **116**, 12123 (2016).
  - [3] X. Zhang and L.-D. Zhao, Thermoelectric materials: Energy conversion between heat and electricity, *J. Materiomics* **1**, 92 (2015).
  - [4] G. A. Slack, Nonmetallic crystals with high thermal conductivity, *J. Phys. Chem. Solids* **34**, 321 (1973).
  - [5] Z. H. U. Tie-Jun, Z. Xin-Bing, X. I. N. Jia-Zhan, F. U. Tie-Zheng, F. Teng, and S. Jia-Jun, Lattice thermal conductivity in thermoelectric materials, *J. Inorg. Mater.* **34**, 260 (2019).
  - [6] C. Chang and L.-D. Zhao, Anharmonicity and low thermal conductivity in thermoelectrics, *Mater. Today Phys.* **4**, 50 (2018).
  - [7] X. Qian, J. Zhou, and G. Chen, Phonon-engineered extreme thermal conductivity materials, *Nat. Mater.* **20**, 1188 (2021).
  - [8] T. Ghosh, M. Dutta, D. Sarkar, and K. Biswas, Insights into low thermal conductivity in inorganic materials for thermoelectrics, *J. Am. Chem. Soc.* **144**, 10099 (2022).
  - [9] J. L. Li, W. Hu, and J. L. Yang, High-throughput screening of rattling-induced ultralow lattice thermal conductivity in semiconductors, *J. Am. Chem. Soc.* **144**, 4448 (2022).
  - [10] W. L. Ong, S. M. Rupich, D. V. Talapin, A. J. McGaughey, and J. A. Malen, Surface chemistry mediates thermal transport in three-dimensional nanocrystal arrays, *Nat. Mater.* **12**, 410 (2013).
  - [11] W. L. Ong, E. S. O'Brien, P. S. Dougherty, D. W. Paley, C. F. Higgs III, A. J. McGaughey, J. A. Malen, and X. Roy, Orientational order controls crystalline and amorphous thermal transport in superatomic crystals, *Nat. Mater.* **16**, 83 (2017).
  - [12] *Superatoms: Principles, Synthesis and Applications*, edited by P. Jena and Q. Sun (Wiley & Sons Ltd, Chichester, UK, 2021), pp. 1–7.
  - [13] S. N. Khanna and P. Jena, Assembling Crystals from Clusters, *Phys. Rev. Lett.* **69**, 1664 (1992).
  - [14] S. N. Khanna and P. Jena, Atomic clusters: Building blocks for a class of solids, *Phys. Rev. B* **51**, 13705 (1995).
  - [15] P. Jena and Q. Sun, Super atomic clusters: Design rules and potential for building blocks of materials, *Chem. Rev.* **118**, 5755 (2018).
  - [16] Q. Zhang, Y. Gao, R. Wang, Y. Zhu, W. Xie, G. Schreckenbach, and Z. Wang, Interaction potential energy surface between superatoms, *Chem. Commun.* **56**, 14681 (2020).
  - [17] M. Christensen, A. B. Abrahamsen, N. B. Christensen, F. Juranyi, N. H. Andersen, K. Lefmann, J. Andreasson, C. R. Bahl, and B. B. Iversen, Avoided crossing of rattler modes in thermoelectric materials, *Nat. Mater.* **7**, 811 (2008).
  - [18] D. J. Voneshen, K. Refson, E. Borissenko, M. Krisch, A. Bosak, A. Piovano, E. Cemal, M. Enderle, M. J. Gutmann, M. Hoesch *et al.*, Suppression of thermal conductivity by rattling modes in thermoelectric sodium cobaltate, *Nat. Mater.* **12**, 1028 (2013).
  - [19] T. M. Tritt, Holey and unholey Semiconductors, *Science* **283**, 804 (1999).
  - [20] M. M. Koza, M. R. Johnson, R. Viennois, H. Mutka, L. Girard, and D. Ravot, Breakdown of phonon glass paradigm in La- and Ce-filled Fe<sub>4</sub>Sb<sub>12</sub> skutterudites, *Nat. Mater.* **7**, 805 (2008).

- [21] S. Kumar, C. Shao, S. Lu, and A. J. H. McGaughey, Contributions of different degrees of freedom to thermal transport in the C<sub>60</sub> molecular crystal, *Phys. Rev. B* **97**, 104303 (2018).
- [22] X. Roy *et al.*, Nanoscale atoms in solid-state chemistry, *Science* **341**, 157 (2013).
- [23] P. Gougeon *et al.*, Synthesis, crystal and electronic structures, and thermoelectric properties of the novel cluster compound Ag<sub>3</sub>In<sub>2</sub>Mo<sub>15</sub>Se<sub>19</sub>, *Chem. Mater.* **24**, 2899 (2012).
- [24] P. Gougeon, P. Gall, S. Misra, A. Dauscher, C. Candolfi, and B. Lenoir, Synthesis, crystal structure and transport properties of the cluster compounds Tl<sub>2</sub>Mo<sub>15</sub>S<sub>19</sub> and Ag<sub>3</sub>Tl<sub>2</sub>Mo<sub>15</sub>S<sub>19</sub>, *Mater. Res. Bull.* **136**, 111152 (2021).
- [25] A. Sussardi, T. Tanaka, A. U. Khan, L. Schlapbach, and T. Mori, Enhanced thermoelectric properties of samarium boride, *J. Materiomics* **1**, 196 (2015).
- [26] T. Mori, Thermoelectric and magnetic properties of rare earth borides: Boron cluster and layered compounds, *J. Solid State Chem.* **275**, 70 (2019).
- [27] R. C. Yu, N. Tea, M. B. Salamon, D. Lorents, and R. Malhotra, Thermal Conductivity of Single Crystal C<sub>60</sub>, *Phys. Rev. Lett.* **68**, 2050 (1992).
- [28] J. R. Olson, K. A. Topp, and R. O. Pohl, Specific heat and thermal conductivity of solid fullerenes, *Science* **259**, 1145 (1993).
- [29] X. Wang, C. D. Liman, N. D. Treat, M. L. Chabinyk, and D. G. Cahill, Ultralow thermal conductivity of fullerene derivatives, *Phys. Rev. B* **88**, 075310 (2013).
- [30] J. Nuss, U. Wedig, W. Xie, P. Yordanov, J. Bruin, R. Hübner, A. Weidenkaff, and H. Takagi, Phosphide-tetrahedrite Ag<sub>6</sub>Ge<sub>10</sub>P<sub>12</sub>: Thermoelectric performance of a long-forgotten silver-cluster compound, *Chem. Mater.* **29**, 6956 (2017).
- [31] S. Giri, S. Behera, and P. Jena, Superalkalis and superhalogens as building blocks of supersalts, *J. Phys. Chem. A* **118**, 638 (2014).
- [32] T. Li, P.-H. Du, L. Bai, Q. Sun, and P. Jena, NaNO<sub>3</sub> monolayer: A stable graphenelike supersalt with strong four-phonon scattering and low lattice thermal conductivity insensitive to temperature, *Phys. Rev. Mater.* **6**, 064009 (2022).
- [33] P.-H. Du, C. Zhang, J. Sun, T. Li, and Q. Sun, Phase stability, strong four-phonon scattering, and low lattice thermal conductivity in superatom-based superionic conductor Na<sub>3</sub>OBH<sub>4</sub>, *ACS Appl. Mater. Interfaces* **14**, 47882 (2022).
- [34] T. Li, P.-H. Du, L. Bai, Q. Sun, and P. Jena, Thermoelectric Figure of Merit of a Superatomic Crystal Re<sub>6</sub>Se<sub>8</sub>I<sub>2</sub> Monolayer, *Phys. Rev. Appl.* **18**, 064067 (2022).
- [35] Y. Gao, M. Wu, and P. Jena, A family of ionic supersalts with covalent-like directionality and unconventional multiferroicity, *Nat. Commun.* **12**, 1331 (2021).
- [36] G. Kresse and J. Furthmüller, Efficient iterative schemes for *ab initio* total-energy calculations using a plane-wave basis set, *Phys. Rev. B* **54**, 11169 (1996).
- [37] P. E. Blöchl, Projector augmented-wave method, *Phys. Rev. B* **50**, 17953 (1994).
- [38] G. Kresse and D. Joubert, From ultrasoft pseudopotentials to the projector augmented-wave method, *Phys. Rev. B* **59**, 1758 (1999).
- [39] J. P. Perdew, A. Ruzsinszky, G. I. Csonka, O. A. Vydrov, G. E. Scuseria, L. A. Constantin, X. Zhou, and K. Burke, Restoring the Density-Gradient Expansion for Exchange in Solids and Surfaces, *Phys. Rev. Lett.* **100**, 136406 (2008).
- [40] S. Grimme, J. Antony, S. Ehrlich, and H. Krieg, A consistent and accurate *ab initio* parametrization of density functional dispersion correction (DFT-D) for the 94 elements H-Pu, *J. Chem. Phys.* **132**, 154104 (2010).
- [41] See Supplemental Material at <http://link.aps.org/supplemental/10.1103/PhysRevB.107.155204> for parameters test for DFT, machine-learning potential, NEP-MD simulations of lattice thermal conductivity, force constants fitted by machine learning, parameters test for PBTE solver, atomic equilibrium positions, electron population analysis, potential energy surface, lattice dynamics, elastic properties, AIMD simulations, and phonon thermal transport properties.
- [42] Z. Fan, Z. Zeng, C. Zhang, Y. Wang, K. Song, H. Dong, Y. Chen, and T. Ala-Nissila, Neuroevolution machine learning potentials: Combining high accuracy and low cost in atomistic simulations and application to heat transport, *Phys. Rev. B* **104**, 104309 (2021).
- [43] F. Eriksson, E. Fransson, and P. Erhart, The HIPHIVE package for the extraction of high-order force constants by machine learning, *Adv. Theory Simul.* **2**, 1800184 (2019).
- [44] Z. Fan, H. Dong, A. Harju, and T. Ala-Nissila, Homogeneous nonequilibrium molecular dynamics method for heat transport and spectral decomposition with many-body potentials, *Phys. Rev. B* **99**, 064308 (2019).
- [45] Z. Fan, W. Chen, V. Vierimaa, and A. Harju, Efficient molecular dynamics simulations with many-body potentials on graphics processing units, *Comput. Phys. Commun.* **218**, 10 (2017).
- [46] X. Gu, Z. Fan, and H. Bao, Thermal conductivity prediction by atomistic simulation methods: Recent advances and detailed comparison, *J. Appl. Phys.* **130**, 210902 (2021).
- [47] A. Togo and I. Tanaka, First principles phonon calculations in materials science, *Scr. Mater.* **108**, 1 (2015).
- [48] Y. Le Page and P. Saxe, Symmetry-general least-squares extraction of elastic data for strained materials from *ab initio* calculations of stress, *Phys. Rev. B* **65**, 104104 (2002).
- [49] O. L. Anderson, A simplified method for calculating the Debye temperature from elastic constants, *J. Phys. Chem. Solids* **24**, 909 (1963).
- [50] W. Li, J. Carrete, N. A. Katcho, and N. Mingo, SHENGBTE: A solver of the Boltzmann transport equation for phonons, *Comput. Phys. Commun.* **185**, 1747 (2014).
- [51] Z. Han, X. Yang, W. Li, T. Feng, and X. Ruan, FOUR-PHONON: An extension module to SHENGBTE for computing four-phonon scattering rates and thermal conductivity, *Comput. Phys. Commun.* **270**, 108179 (2022).
- [52] B. Silvi and A. Savin, Classification of chemical bonds based on topological analysis of electron localization functions, *Nature (London)* **371**, 683 (1994).
- [53] V. L. Deringer, A. L. Tchougréeff, and R. Dronskowski, Crystal orbital Hamilton population (COHP) analysis as projected from plane-wave basis sets, *J. Phys. Chem. A* **115**, 5461 (2011).
- [54] Y. Luo *et al.*, Thermoelectric performance of the 2D Bi<sub>2</sub>Si<sub>2</sub>Te<sub>6</sub> semiconductor, *J. Am. Chem. Soc.* **144**, 1445 (2022).
- [55] F. Mouhat and F.-X. Coudert, Necessary and sufficient elastic stability conditions in various crystal systems, *Phys. Rev. B* **90**, 224104 (2014).
- [56] I. R. Shein and A. L. Ivanovskii, Elastic properties of mono- and polycrystalline hexagonal AlB<sub>2</sub>-like diborides of *s*, *p* and *d* metals from first-principles calculations, *J. Phys.: Condens. Matter* **20**, 415218 (2008).

- [57] M. E. Eberhart and T. E. Jones, Cauchy pressure and the generalized bonding model for nonmagnetic bcc transition metals, *Phys. Rev. B* **86**, 134106 (2012).
- [58] S. F. Pugh, XCII. Relations between the elastic moduli and the plastic properties of polycrystalline pure metals, *Philos. Mag.* **45**, 823 (1954).
- [59] M. Rabiei, A. Palevicius, A. Dashti, S. Nasiri, A. Monshi, A. Vilkauskas, and G. Janusas, Measurement modulus of elasticity related to the atomic density of planes in unit cell of crystal lattices, *Materials* **13**, 4380 (2020).
- [60] A. Jain *et al.*, Commentary: The Materials Project: A materials genome approach to accelerating materials innovation, *APL Mater.* **1**, 011002 (2013).
- [61] F. Grønbold and E. F. Westrum, Silver(I) sulfide:  $\text{Ag}_2\text{S}$  heat capacity from 5 to 1000 K, thermodynamic properties, and transitions, *J. Chem. Thermodyn.* **18**, 381 (1986).
- [62] Y. He, T. Day, T. Zhang, H. Liu, X. Shi, L. Chen, and G. J. Snyder, High thermoelectric performance in non-toxic earth-abundant copper sulfide, *Adv. Mater.* **26**, 3974 (2014).
- [63] Y. Zhang, X. Ke, P. R. Kent, J. Yang, and C. Chen, Anomalous Lattice Dynamics near the Ferroelectric Instability in  $\text{PbTe}$ , *Phys. Rev. Lett.* **107**, 175503 (2011).
- [64] K. Ran, R. Zhong, T. Chen, Y. Gan, J. Wang, B. L. Winn, A. D. Christianson, S. Li, Z. Ma, S. Bao *et al.*, Unusual phonon density of states and response to the superconducting transition in the In-doped topological crystalline insulator  $\text{Pb}_{0.5}\text{Sn}_{0.5}\text{Te}$ , *Phys. Rev. B* **97**, 220502(R) (2018).
- [65] M. D. Nielsen, V. Ozolins, and J. P. Heremans, Lone pair electrons minimize lattice thermal conductivity, *Energy Environ. Sci.* **6**, 570 (2013).
- [66] M. Dutta, K. Pal, U. V. Waghmare, and K. Biswas, Bonding heterogeneity and lone pair induced anharmonicity resulted in ultralow thermal conductivity and promising thermoelectric properties in  $n$ -type  $\text{AgPbBiSe}_3$ , *Chem. Sci.* **10**, 4905 (2019).
- [67] I. Errea, M. Calandra, and F. Mauri, Anharmonic free energies and phonon dispersions from the stochastic self-consistent harmonic approximation: Application to platinum and palladium hydrides, *Phys. Rev. B* **89**, 064302 (2014).
- [68] F. Zhou, W. Nielson, Y. Xia, and V. Ozolins, Lattice Anharmonicity and Thermal Conductivity from Compressive Sensing of First-Principles Calculations, *Phys. Rev. Lett.* **113**, 185501 (2014).
- [69] Z. Z. Zeng, C. Z. Zhang, Y. Xia, Z. Y. Fan, C. Wolverton, and Y. Chen, Nonperturbative phonon scatterings and the two-channel thermal transport in  $\text{Tl}_3\text{VSe}_4$ , *Phys. Rev. B* **103**, 224307 (2021).
- [70] M. Samanta, K. Pal, P. Pal, U. V. Waghmare, and K. Biswas, Localized vibrations of Bi bilayer leading to ultralow lattice thermal conductivity and high thermoelectric performance in weak topological insulator  $n$ -type  $\text{BiSe}$ , *J. Am. Chem. Soc.* **140**, 5866 (2018).
- [71] P. B. Allen, X. Du, L. Mihaly, and L. Forro, Thermal conductivity of insulating  $\text{Bi}_2\text{Sr}_2\text{YCu}_2\text{O}_8$  and superconducting  $\text{Bi}_2\text{Sr}_2\text{CaCu}_2\text{O}_8$ : Failure of the phonon-gas picture, *Phys. Rev. B* **49**, 9073 (1994).
- [72] J. L. Feldman, P. B. Allen, and S. R. Bickham, Numerical study of low-frequency vibrations in amorphous silicon, *Phys. Rev. B* **59**, 3551 (1999).
- [73] S. Mukhopadhyay, D. S. Parker, B. C. Sales, A. A. Puretzy, M. A. McGuire, and L. Lindsay, Two-channel model for ultralow thermal conductivity of crystalline  $\text{Tl}_3\text{VSe}_4$ , *Science* **360**, 1455 (2018).
- [74] Z. Zeng, C. Zhang, H. Yu, W. Li, Y. Pei, and Y. Chen, Ultralow and glass-like lattice thermal conductivity in crystalline  $\text{BaAg}_2\text{Te}_2$ : Strong fourth-order anharmonicity and crucial diffusive thermal transport, *Mater. Today Phys.* **21**, 100487 (2021).
- [75] M. Simoncelli, N. Marzari, and F. Mauri, Unified theory of thermal transport in crystals and glasses, *Nat. Phys.* **15**, 809 (2019).
- [76] Y. S. Touloukian, P. E. Liley, and S. C. Saxena, in *Thermophysical Properties of Matter* (IFI/Plenum, New York, 1970).
- [77] T. Feng, L. Lindsay, and X. Ruan, Four-phonon scattering significantly reduces intrinsic thermal conductivity of solids, *Phys. Rev. B* **96**, 161201(R) (2017).
- [78] X. Chen, D. Wang, X. Liu, L. Li, and B. Sanyal, Two-dimensional square- $A_2B$  ( $A = \text{Cu, Ag, Au}$ , and  $B = \text{S, Se}$ ): auxetic semiconductors with high carrier mobilities and unusually low lattice thermal Conductivities, *J. Phys. Chem. Lett.* **11**, 2925 (2020).
- [79] A. Kundu, X. Yang, J. Ma, T. Feng, J. Carrete, X. Ruan, G. K. H. Madsen, and W. Li, Ultrahigh Thermal Conductivity of  $\theta$ -Phase Tantalum Nitride, *Phys. Rev. Lett.* **126**, 115901 (2021).
- [80] J. Sun, C. Zhang, Z. Yang, Y. Shen, M. Hu, and Q. Wang, Four-phonon scattering effect and two-channel thermal transport in two-dimensional paraelectric  $\text{SnSe}$ , *ACS Appl. Mater. Interfaces* **14**, 11493 (2022).
- [81] K. Pal, Y. Xia, and C. Wolverton, Microscopic mechanism of unusual lattice thermal transport in  $\text{TlInTe}_2$ , *npj Comput. Mater.* **7**, 5 (2021).